# Desktop-level Small Automatic Guided Vehicle Driven by a Liquid Metal Droplet

Zhenyou Ge ‡[a], Wenshang Guo ‡[a], Ye Tao *[ab], Weiyu Liu [c], Rui Xue [a], Chunlei Song [a], Hongyuan Jiang [d], Yukun Ren *[a]

a. *State Key Laboratory of Robotics and System, Harbin Institute of Technology, West Da-zhi Street 92, Harbin, Heilongjiang 150001, People's Republic of China.*

b. *School of Engineering and Applied Sciences and Department of Physics Harvard University, 9 Oxford Street, Cambridge, MA 02138, USA.*

c. *Chang'an University, Middle-Section of Nan'er Huan Road, Xi'an 710000, China*

d. *School of Mechatronics Engineering, Harbin Institute of Technology, West Da-zhi Street 92, Harbin 150001, People's Republic of China.*

\* *Corresponding author.*

*E-mail addresses: ytao@seas.harvard.edu (Ye Tao)*

*rykhit@hit.edu.cn (Yukun Ren)*

‡ *These authors contributed equally to this work.*

# Supplementary Information Appendix

**SI Appendix 1. Design and fabrication information of the armor.**

The armor is the shell of the small traction vehicle and the height of all armor is 14 mm. The existence of the armor not only formed certain protection to the flexible liquid metal (LM) but also provided a basic component, which could realize different small operation functions by installing different mechanical transmission components on it.
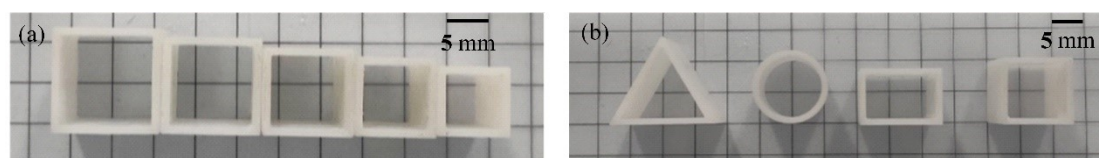


**Fig. S1** Different forms of armor. (a) Different sizes of armor. (b) Different shapes of armor.

500 μL liquid metal (LM) droplet was assembled with different shapes of armor (Fig. S1) in a glass container containing 2 mol/L NaOH solution. We first placed the armor on the container operating platform with a tweezer. A liquid metal droplet was then added to the armor by a pipette gun easily. The LM droplet was limited by the shape of the armor, and under the effect of interfacial tension, different LM shapes were formed in different armors. We took pictures from the top and bottom of the armor respectively, as shown in Fig. S2.
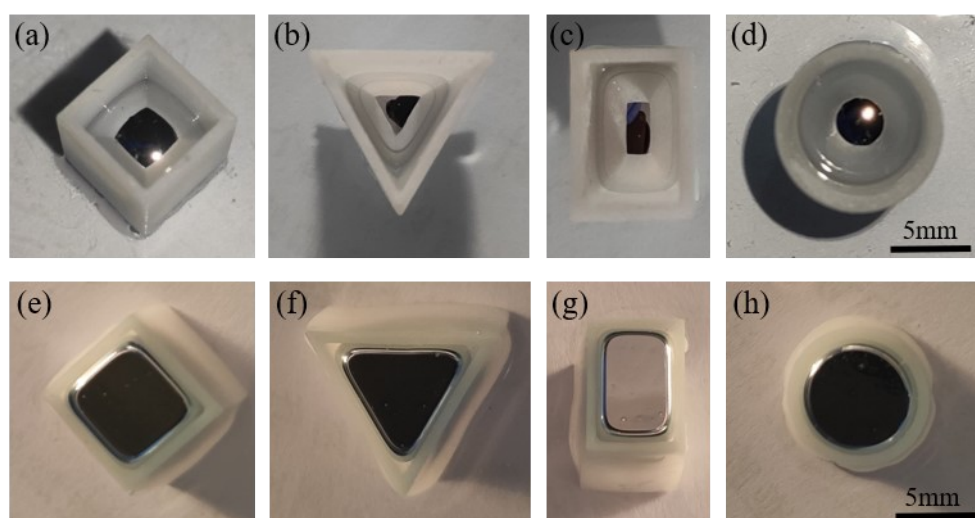


**Fig. S2** Static images of the LM droplet shape with armor in NaOH solution. (a)-(d) The top views of the LM droplet in the square, triangle, rectangle, circle armor. (e)-(h) The bottom views of the LM droplet in the square, triangle, rectangle, circle armor.


**SI Appendix 2. The hardware part of the desktop-level sAGV system**

The hardware part of the small automatic guided vehicle (sAGV) system was shown in Fig. S3(a). 16 graphite electrodes were arranged around the glass container as shown in Fig. S3(b). An industrial camera was set up on the top of the glass container through the camera bracket to realize the position detection and track recording of the vehicle, as shown in Fig. S3(c). The 16 graphite electrodes were connected with the 32-channel

network relay control module for electrodes on-off control. A DC power supply was used to connect the splitter to realize different supply voltages for the 16 electrodes according to different application scenarios. The 32-channel network relay control module was operated at the voltage of 12 V and was powered by an AC-DC switch power supply, as shown in Fig. S3(d).
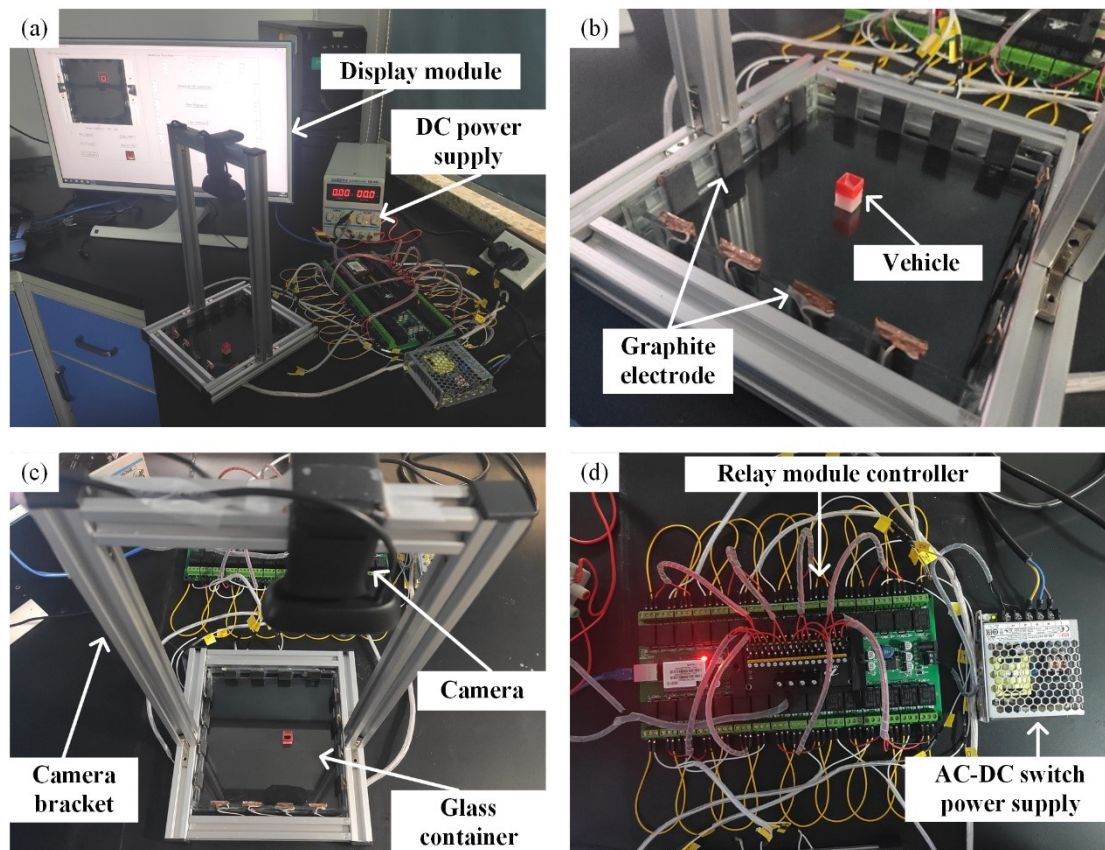


**Fig. S3** Detailed composition and description of each part. (a) The overall physical view of the hardware system. (b) The operation platform of the small traction vehicle. (c) The installation of an industrial camera and camera bracket. (d) The 32-channel network relay control module and its power supply.

**SI Appendix 3. The software part of the desktop-level sAGV system**

The actual Graphical User Interface (GUI) was shown in Fig. S4. The image was collected by the camera and displayed on the interface of the real-time image display module. There were corresponding operation buttons in the user basic operation module to control the opening and closing of the camera. When it is necessary to detect and track the position of the vehicle, the target image to be detected should be given by selecting the detection image button. And then the program could search and recognize the target through the image recognition algorithm. The detected target was marked in the form of a red box, and the real-time coordinate of the vehicle was displayed below the image display module. The position information of the vehicle is displayed in the form of pixel coordinates, and the resolution of the picture taken by the camera is 640×480 px. The viewable area of the camera is 170×128 mm, and the pixel pitch is 0.266 mm. The on-off states of the 16 electrodes were displayed on the operation panel.

Each electrode had three states: floating, positive potential, and grounding, corresponding to white, red and gray marks respectively. The state of the electrode can be determined by clicking the button. When the program was under automatic control, the electrode panel will display the state information of the electrode in real-time. Before operating the operation panel, it is necessary to establish the communication relationship between the control module and the drive module. Click the "establish TCP connection" button on the operation panel to realize the communication connection between the two modules. The trajectory path can be selected to realize the automatic control of vehicle movement by clicking the "Path selection" button.
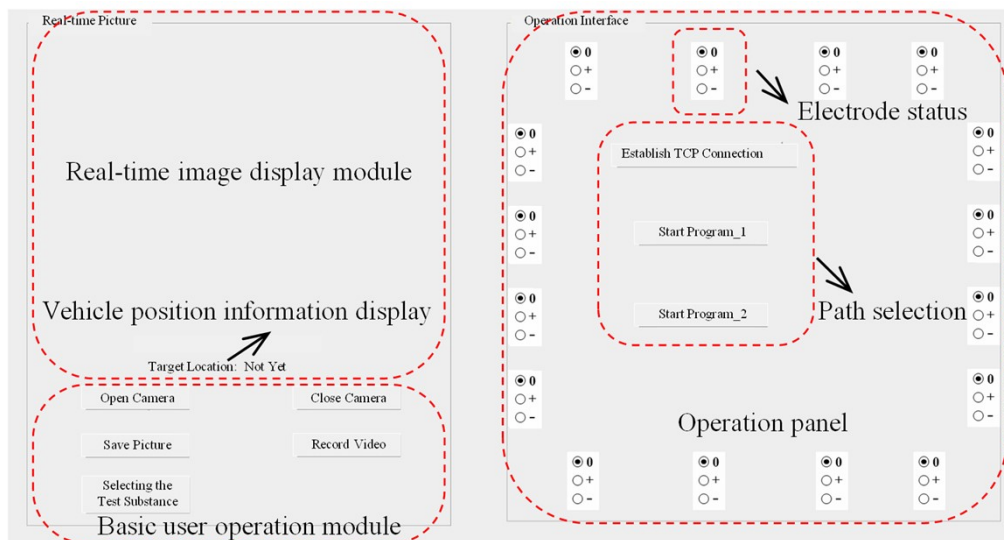


**Fig. S4** The Graphical User Interface of the sAGV system.

The visual recognition module can realize the function of extracting the position of the vehicle and tracking the movement in real-time, mainly through the visual recognition algorithm. In this paper, the image recognition algorithm was a template matching algorithm, which was written by python language.

In the template matching algorithm, two images were needed: the first was the template image that needed to be found; the second was the original image that needed to be detected and contains the desired template matching area. The main principle was to slide the template image block (Fig. S5(b)) on the input image (Fig. S5(a)) to match, and the function cvMinMaxLoc() can be used to find the best matching position. The ultimate goals were to detect the best matching area and mark the detection result with a red box, as shown in Fig. S5(c).

Vehicles in different locations were separately tested for identification, and the test results were shown in Fig. S5(d). In the process of recognition, visual recognition had high accuracy for oblique images or deformed images. Therefore, the template matching algorithm had high recognition accuracy in the test and met the requirements of the identification accuracy in the complex and changeable environment.
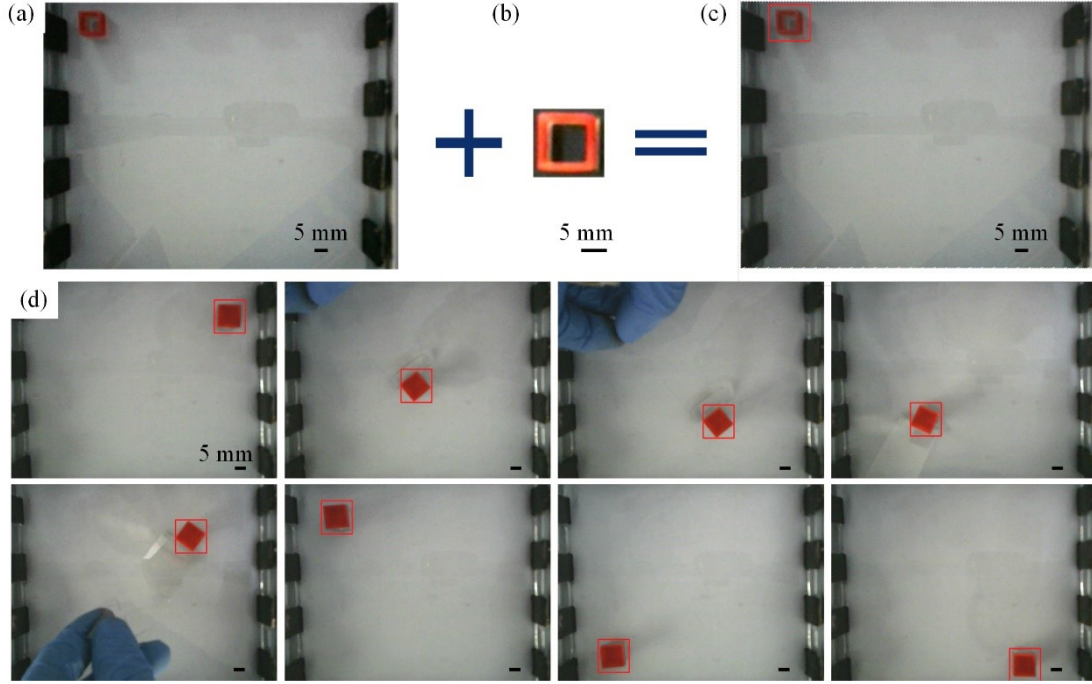
**Fig. S5** The principle and effect of visual recognition. (a) The original image to be detected. (b) The target image to be found. (c) The resulting image with the target image marked by the red box. (d) The visual recognition renderings of the target in different locations.

**SI Appendix 4: Theoretical background and the deduction details of fluid flow velocity**

The relationship between the interfacial tension and the potential difference is described by Lippmann's equation:

$$\gamma = \gamma_0 - \frac{1}{2}CV^2 \qquad (S1)$$

where $\gamma$ is the interfacial tension, $C$ is the capacitance of the electric double layer (EDL) per unit area, $V$ is the potential difference across the EDL, and $\gamma_0$ is the maximum interfacial tension at $V=0$.

When no external electric field is applied, the EDL capacitance on the LM surface is charged due to the transfer of electrons and ions, as shown in Fig. 2(a). Assuming that there is no interference, the surface charge density $q_0$ is uniformly distributed along the surface. The potential difference $V_0$ across the native electric double layer (NDL) is determined by the degree of ion adsorption:

$$V_0 = -\frac{q_0}{C} \qquad (S2)$$

When an electric field is applied, the dipole Debye shielding charge is attracted to the LM surface, generating the induced electric double layer (IDL) charge on the surface, as shown in Fig. S6. Because charged ionic in the electrolyte solution cannot enter the LM phase through the surface, the Ohmic current and the diffusion current balance each other at the interface. Therefore, within the limit of the thin boundary layer and small zeta potential, the normal Ohm current injected from the fluid should be

continuous with the displacement current through the IDL on the conductive droplet.

$$\sigma \boldsymbol{n} \cdot \nabla \phi_{DC} = 0 \tag{S3}$$

$$\phi_{DC}^0 = \frac{\int_{\partial drop} \phi_{DC} dS}{\int_{\partial drop} dS} \tag{S4}$$

where $\sigma$ is the dielectric conductivity, $\boldsymbol{n}$ is the unit normal vector on the LM surface drop, $\Phi_{DC}$ is the DC potential of the NaOH solution, and $\Phi_{DC}^0$ is the corresponding transient body voltage of the conducting droplet affected respectively by the DC voltage component.
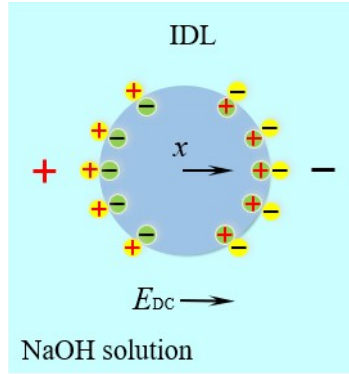


**Fig. S6** Induced charge distribution of the EGaIn droplet surface when an external electric field is applied.

Therefore, due to the existence of an external electric field, the IDL potential difference $V_1$ is formed between the electrolyte solution and the LM:

$$V_1 = \phi_{DC}^0 - \phi_{DC} \tag{S5}$$

The superposition of NDL and IDL produces a new charge distribution (shown in Fig. 2(b)). The composite potential difference $V$ across the EDL is obtained by the superposition principle in electrochemistry:

$$V = V_0 + V_1 = -\frac{q_0}{C} + \left( \phi_{DC}^0 - \phi_{DC} \right) \tag{S6}$$

As shown in Fig.S6, the x-coordinate is centered on the LM and in the positive direction along the electric field. Assuming that the LM extends infinitely along the x-direction under one-dimensional approximation, the expression of the potential difference can be obtained:

$$\phi_{DC} - \phi_{DC}^0 = -E_{DC} x \tag{S7}$$

where the $E_{DC}$ is the electric field intensity in the solution.

The expression of the interfacial tension gradient can be obtained by substituting the equation (S2), (S6), and (S7) into the equation (S1).

$$\gamma = \gamma_0 - \frac{1}{2}C\left(-\frac{q_0}{C} + E_{DC}x\right)^2$$

$$= \gamma_0 - \frac{1}{2}C\left(\frac{q_0^2}{C^2} + E_{DC}^2 x^2 - \frac{2q_0 E_{DC}}{C}x\right) \tag{S8}$$

Fluid physics in continuous electrowetting (CEW) is essentially a problem of transient two-phase flow at the metal-electrolyte interface driven by electrocapillary surface stress. The flow behavior of incompressible Newtonian fluids is controlled by the Navier-Stokes equation:

$$\nabla \cdot \boldsymbol{u} = 0 \tag{S9}$$

$$\rho\frac{\partial u}{\partial t} + \rho(\boldsymbol{u}\cdot\nabla)\boldsymbol{u} = \nabla\cdot[-p + \eta\nabla\boldsymbol{u}] + \boldsymbol{F} \tag{S10}$$

where $\rho$ and $\eta$ denote the mass density and dynamic viscosity of the corresponding medium, $p$ is the scalar field of hydraulic pressure, and $\boldsymbol{u}$ is the vector field of flow velocity. $\boldsymbol{F}$ represents any external body force acting on the fluidic system, and is specifically considered here as gravity, namely, $\boldsymbol{F} = -\rho g e z$, with $\boldsymbol{g} = 9.8$ m/s$^2$ being the gravitational acceleration.

Ignoring the influence of the positive pressure of the solution and the moving viscous force of the droplet, the force balance at the phase boundary refers to the balance of the viscous shear stress $\tau_{LM}$ and the interfacial tension gradient, as well as the local interfacial tension balance under the Laplace pressure of the curved interface:

$$\tau_{LM} = \nabla_t\gamma \tag{S11}$$

$$\Delta p \cdot \boldsymbol{n} = \frac{2\gamma}{R}\cdot\boldsymbol{n} \tag{S12}$$

where $\nabla_t = (\boldsymbol{I} - \boldsymbol{nn})\cdot\nabla$ is the operator of the surface gradient, $\Delta p$ is the difference of static pressure between the conducting droplet phase and the buffer medium phase, $R$ is the principal radius of curvature of the LM droplet.

The electrical Marangoni shear stress is originated by the surface gradient of the interfacial tension:

$$\eta\cdot\frac{\langle\boldsymbol{u}\rangle}{R} = \frac{\partial\gamma}{\partial x} \tag{S13}$$

$$\frac{\partial\gamma}{\partial x} = q_0 E_{DC} - CE_{DC}^2 x \tag{S14}$$

Therefore, fluid flow from low interfacial tension to high interfacial tension will be generated on the LM surface due to the presence of the interfacial tension gradient. The velocity of the fluid near the surface can be obtained by combining equations (S13)

and (S14).

$$\langle \boldsymbol{u} \rangle = \frac{q_0 E_{\mathrm{DC}} R}{\eta} - \frac{C E_{\mathrm{DC}}^2 R}{\eta} x \tag{S15}$$

The LM surface velocity mainly includes the global velocity component $\boldsymbol{u}_{\mathrm{globe}}$ and the local velocity component $\boldsymbol{u}_{\mathrm{local}}$ at different locations:

$$\boldsymbol{u}_{\mathrm{globe}} = \frac{q_0 E_{\mathrm{DC}} R}{\eta} \tag{S16}$$

$$\boldsymbol{u}_{\mathrm{local}} = -\frac{C E_{\mathrm{DC}}^2 R}{\eta} x \tag{S17}$$

**SI Appendix 5. The simulation results and details of the vehicle under electric field.**

The length of the white arrow (shown in Fig. S7(a)) showed the current density on the surface of the LM in detail. The LM had a higher current density at the top and a lower current density around it. From the color distribution in Fig. S7(a), the electric potential of the LM surface illustrated a decreasing trend from left to right, and the local electric potential reached 1.02 V. So the presence of LM affected the variation of local potential in the solution. Influenced by the external electric field, an induced interface potential between the electrolyte solution and the LM was formed by the induced electric double layer. To make the image clear, the induced potential distribution on the LM surface was observed from the top view, as shown in Fig. S7(b). The induced potential presented a gradient distribution characteristic and distributed symmetrically along the cross-section of the two electrodes.
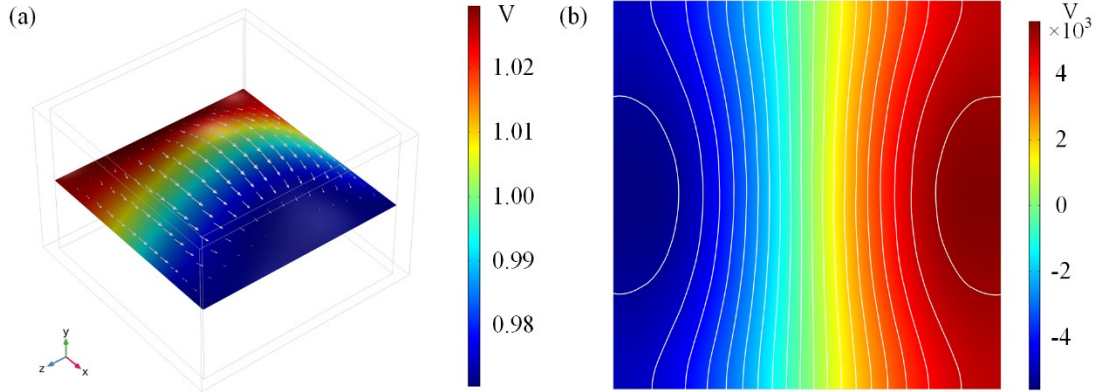


**Fig. S7** The potential changes on the surface of LM. (a) The variation of solution voltage on the LM surface caused by the applied electric field. (b) The induced potential difference across the EDL induced by the external electric field (top view of the surface).

The Marangoni fluid vortex was induced by the interfacial tension gradient in the solution, which produced different flow rates in different areas. Three fluid vortices were formed on the left, right and upper sides of the vehicle, as shown in Fig.S8. Moreover, the fluid velocity on the surface of the LM was the largest, with the maximum flow rate exceeding 0.16 m/s. Therefore, the circulating flow was caused by
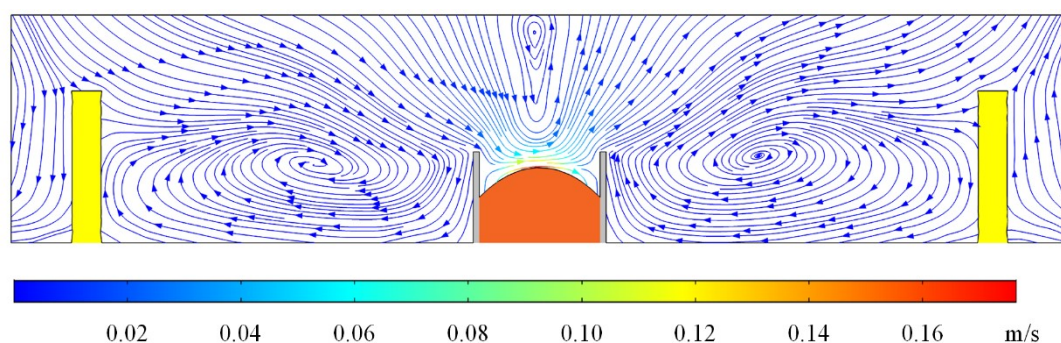
the fluid flow on the surface of the LM.



**Fig. S8** The flow field distribution in the solution passing through the cross-section of the two electrodes.

## SI Appendix 6. Fluid flow on liquid metal surfaces.

In the driving experiment of the square armor, we observed the surface flow of LM from the bottom and top of the armor respectively. The red ink was dripped on one side of the armor to trace the direction of the flow, and a 10 V voltage was applied to drive the LM vehicle to move. As shown in Fig. S9(b), the flow was not observed in the bottom part of LM that contacts the substrate. This indicates that the bottom of the LM is in close contact with the glass surface during the movement of the vehicle. Conversely, the color change of solution and the rising of the liquid level were observed on the top surface of the LM actuator (shown in Fig. S9(c)). This provides direct evidence of fluid flow on top of LM.

In addition, we carried out a control experiment that the LM droplet was topped with a polymer holder to see if the LM droplet still can be actuated in this situation. The polymer holder was 3D printed with transparent photosensitive resin, as shown in Fig. S9(d). Its structure is a blind hole with an opening bottom and a closed top. The cross-sectional view of the structure is shown in Fig. S9(e). When the polymer holder is covered on the top of the LM, the internal curved structure can be perfectly matched to the liquid metal surface. After applying a voltage of 10 V to both ends of the LM, a picture was taken from the bottom of the LM, as shown in Fig. S9(f). The bottom of the LM is closely attached to the surface of the glass, and there is no liquid layer or flow phenomenon between LM and the substrate. Moreover, the LM droplet covered with a polymer holder cannot be actuated.

Therefore, there is no liquid layer between the LM and the glass surface under the action of the gravity of the LM. And the generated flows and the actuation are induced by the top surface of the LM actuator. Through the global flow velocity equation (3), there is a flow in the same direction as the electric field, and it is proportional to the

strength of the electric field. Driven by the flow on the surface of the LM, the solution flows in from the bottom of the armor and out from the other side (shown in Fig.S9(g)). According to Newton's third law, in the process of solution flowing along the direction of the electric field, a reaction force opposite to the flow direction will be generated on the LM surface, driving the vehicle to move towards the anode (shown in Fig. S9(h)).
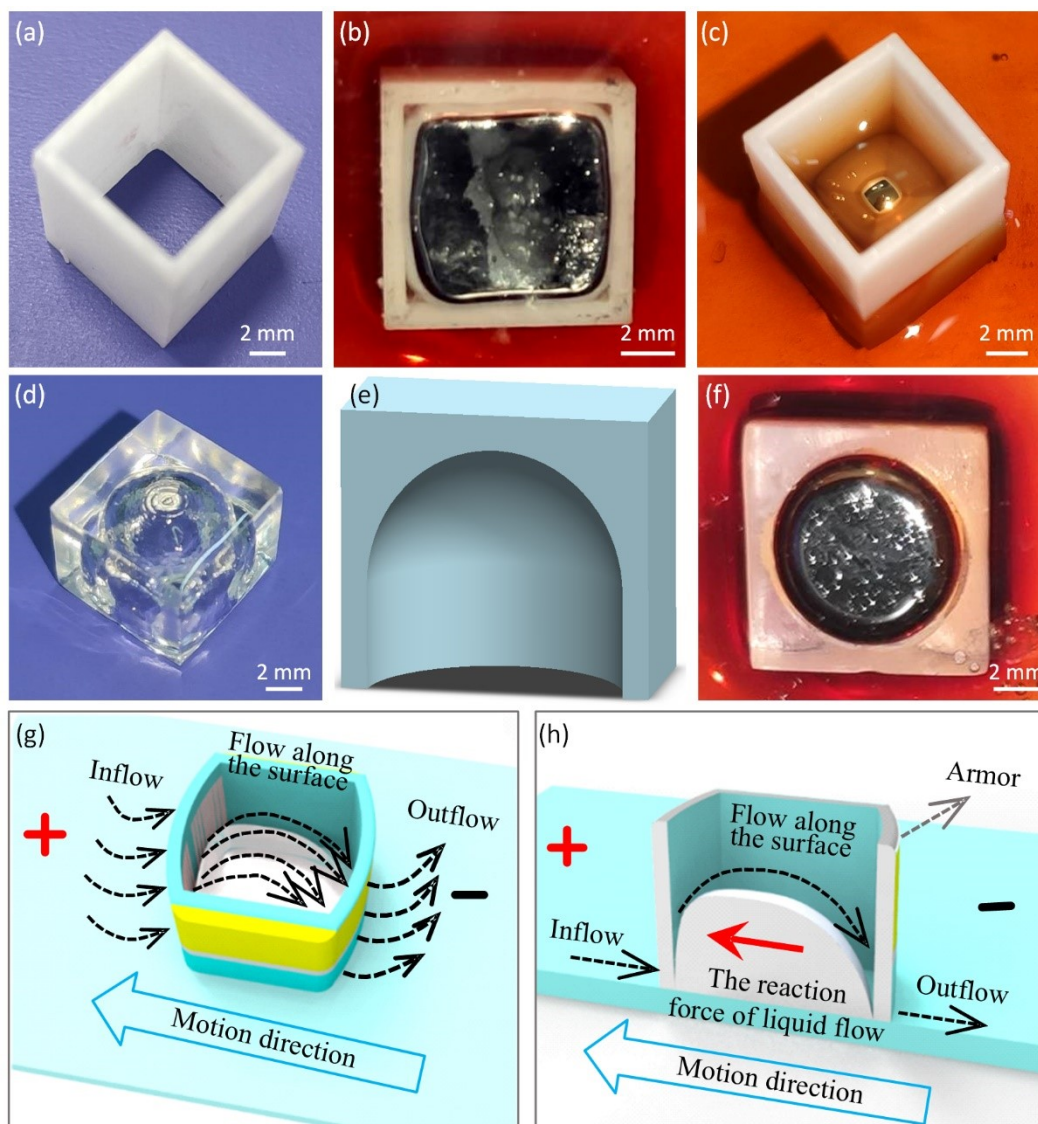


Fig. S9 States of flow at the top and bottom of the LM droplet. (a) The physical picture of through-hole square armor. (b) The bottom surface morphology of the LM with square armor. (c) The top surface morphology of the LM with square armor. (d) The physical image of a polymer holder with a blind hole structure. (e) A cross-sectional view of a polymer holder with a blind hole structure. (f) The bottom surface morphology of the LM that covers the polymer holder. (g) Overall schematic diagram of fluid flow. (h) The reaction force caused by the flow of fluid.

**SI Appendix 7. A detailed explanation of the rotating behavior of the vehicle.**

The rotational motion of the LM droplet had also been observed in the driving experiments of different shapes of armor: when the direction of the two electrodes was not coincident with the symmetry line of the armor, the armor rotated in the process of moving towards the anode electrode (shown in Fig.S10). The difference from the article is that the electrodes used in the rotating motion are cylindrical graphite electrodes with a diameter of 2 mm. The rectangular armor rotates to make the long side approximately parallel to the current direction, as shown in Fig. S10(a). For a vehicle with triangular armor, the vehicle rotates so that one of its corners faces the anode pole, as shown in Fig. S10(b).
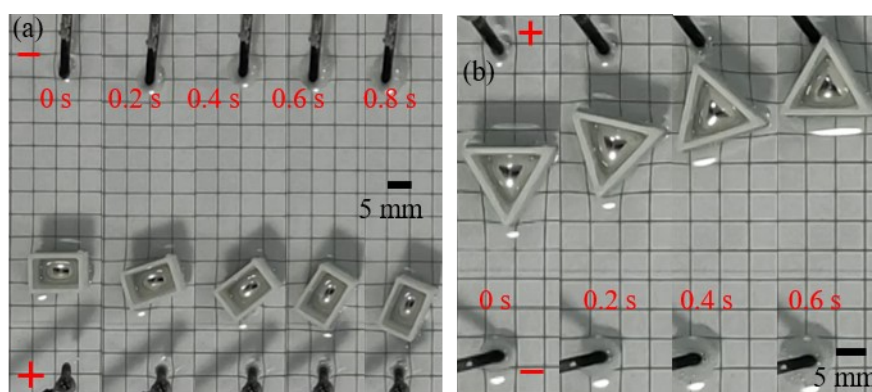


Fig. S10 Rotation phenomenon during vehicle movement. (a) Continuous rotation of LM with rectangular armor. (b) Continuous rotation of LM with triangle armor.

The reasons for the rotation phenomena of LM with rectangular armor and triangular armor were simulated. By simulation analysis, the asymmetric interfacial tension gradient was an important reason for the rotation of rectangular armor and triangular armor.

The DC voltage is applied in a direction perpendicular to the long side of the rectangular armor, where the two electrodes should be connected in a direction that coincides with the symmetrical line of the rectangle, as shown in Fig. S11(a). As can be seen from the interfacial tension gradient diagram (Fig.S12(a)), the driving force generated by the interfacial tension gradient coincides with the connecting direction of the two electrodes. In other words, the driving force coincides with the direction of movement. Therefore, the vehicle with rectangular armor does not rotate as it moves toward the anode pole.

Due to the limitation of test conditions and the existence of test errors, the direction of the two electrodes is difficult to coincide with the symmetry line of the rectangular armor. Therefore, according to the actual situation of the experiment, the arrangement of the two electrodes is offset by 6 mm, as shown in Fig. S11(b). When the two

electrodes were biased, the interfacial tension gradient of the LM was simulated as shown in Fig. S12(b). By analyzing the interfacial tension gradient of offset position, it can be known that the interfacial tension gradient contour has a certain deflection, causing the driving force and the direction of movement to be different. There is a speed difference between the left and right sides of the armor and it rotates.
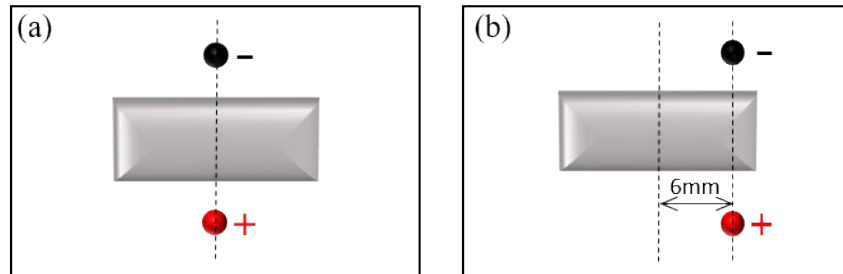


Fig. S11 Diagram of different power-up models of rectangular armor. (a) The direction of the two electrodes' connection coincides with the symmetry line. (b) The direction of the two electrodes' connection is biased to the symmetry line.
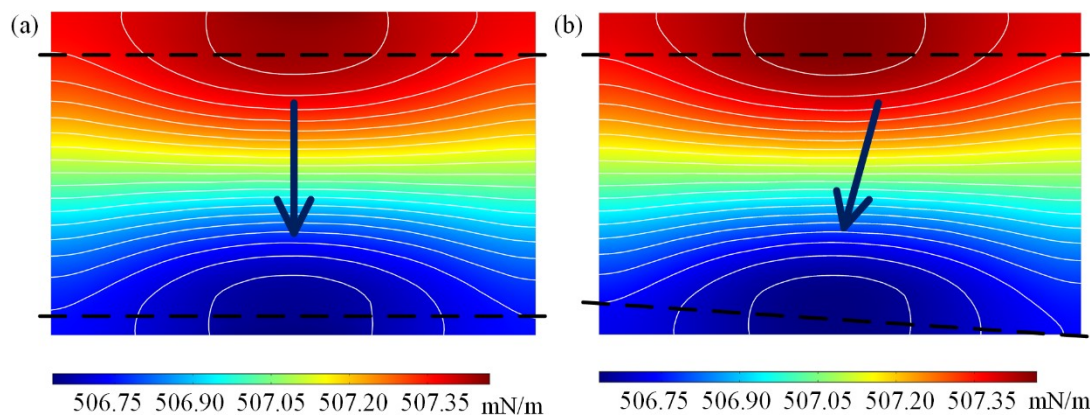


Fig. S12 Interfacial tension gradient of rectangular armor under different power-up models. (a) The interfacial tension gradient is symmetric. (b) The interfacial tension gradient is asymmetric.

The rotation phenomenon of the triangular armor was analyzed in the same way. Apply a voltage in the direction perpendicular to one side of the triangular armor, where the connection direction of the two electrodes should coincide with the high line of the triangle (Fig.S13(a)). And the interfacial tension gradient was obtained by simulation, as shown in Fig.S14(a). When the connection direction of the two electrodes coincides with the symmetry axis of the triangle, a symmetric interfacial tension gradient will be generated. However, when the connection direction of the electrodes does not coincide with the axis of symmetry (Fig.S13(b)), an asymmetric interfacial tension gradient will be generated, as shown in Fig.S14(b). As a result, when the vehicle with triangular armor moves toward the anode electrode, a speed difference will occur on the left and right sides of the armor, causing a rotational motion. Therefore, the asymmetric

interfacial tension gradient is an important reason for the rotation of rectangular armor and triangular armor.
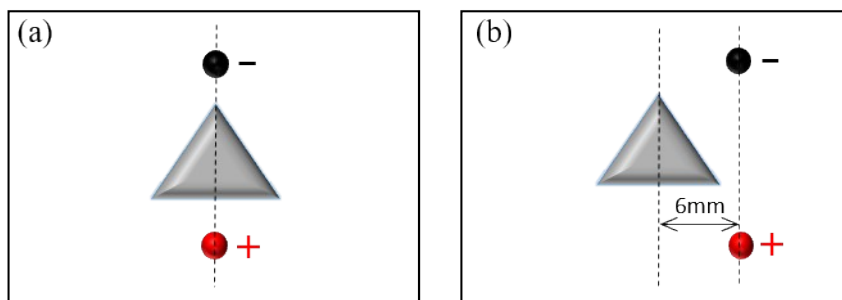


Fig. S13 Diagram of different power-up models of triangular armor. (a) The direction of the two electrodes' connection coincides with the symmetry line. (b) The direction of the two electrodes' connection is biased to the symmetry line.
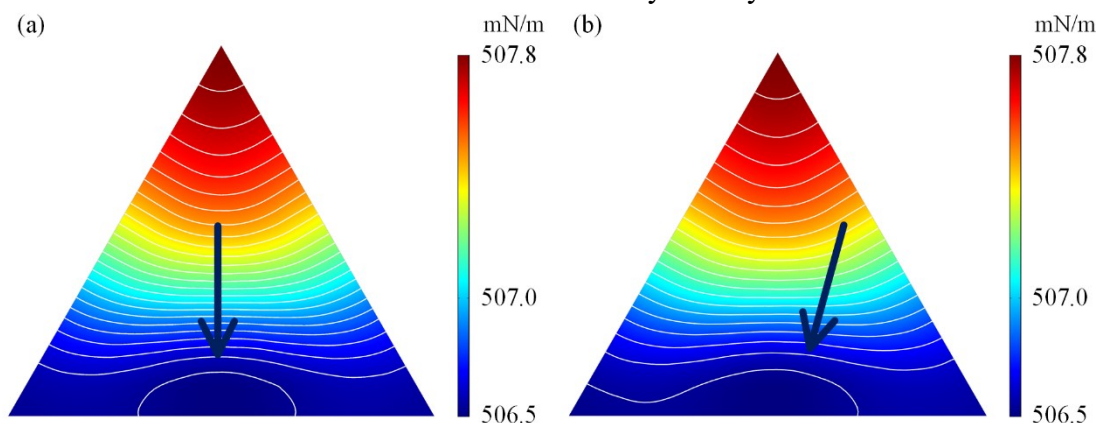


Fig. S14 Interfacial tension gradient of triangular armor under different power-up models. (a) The interfacial tension gradient is symmetric. (b) The interfacial tension gradient is asymmetric.

Besides, the fluid resistance during vehicle movement and the deformation of droplets are other important causes of rotation. For rectangular armor and triangular armor, the liquid metal vehicles move in the direction of least fluid resistance during the linear movement. The lengthening effect of the LM droplet under the action of an electric field may also cause the armor to rotate.

As a result, the armor rotated in the process of moving towards the anode electrode. Therefore, we can adjust the posture of the liquid metal vehicle by changing the angle between the electrode connection and the armor. In this work, we mainly used the square armored vehicle for trajectory driving and cargo transportation. For square armor, the attitude of the armor has little effect on the movement of the vehicle. Flake graphite electrodes are also used in the experiment to avoid the rotation phenomenon. The translation motion of the liquid metal droplet could enable the successful kicking off of the cargos.

**SI Appendix 8. Design and fabrication information of the cargo storage areas.**

Three cargo storage areas were added to the operating platform of the glass container, as shown in Fig. S15 (a). The storage areas were designed as the V-shaped opening structure with a thickness of 0.8 mm and made by 3D printing with photosensitive resin material. The V-shaped structures were pasted on the bottom of the glass container with glue. To achieve the effect of dispersion, the three V-shaped structures were arranged in a triangular array and presented a smiling face shape. The storage areas 'A' and 'B' were on the same horizontal line, 5 cm apart; the storage area 'C' was vertically separated from the storage areas 'A' and 'B' by 5.5 cm, located at the centerline of the storage areas 'A' and 'B'; the steel balls were placed in the center of the operation platform. Starting from a fixed position, the vehicle transported three steel balls to the three storage areas in turn to realize the function of cargos transportation. The final rendering of the transportation of cargos was shown in Fig. S15(b).
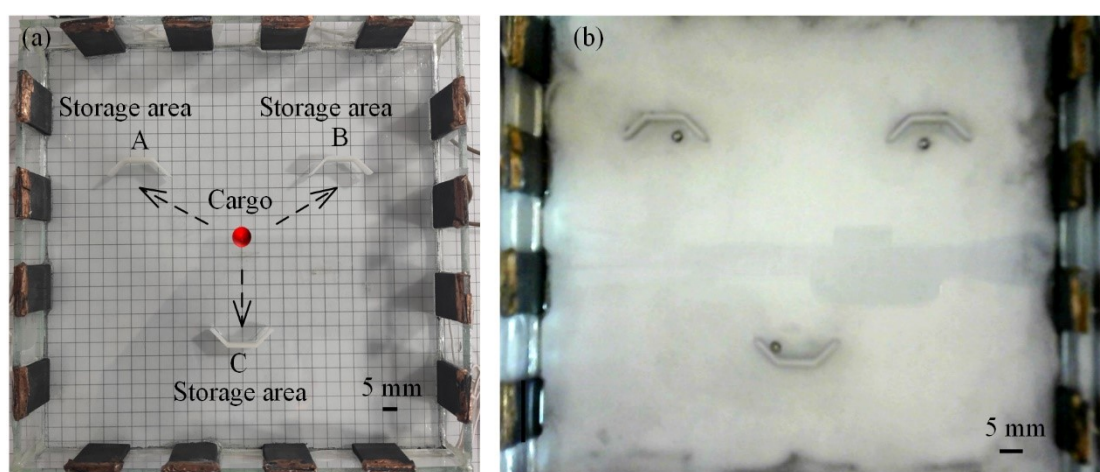


**Fig. S15** An operating platform with cargo storage areas. (a) The top view of the storage areas. (b) The effect picture of cargos stored in the storage areas.

**SI Appendix 9. Extended applications based on the presented platform.**

It is worth mentioning that the small traction vehicle has advantages in cargo transportation in a liquid environment. If the cargos cannot be compatible in an alkaline solution, a cargo platform that can be installed on the top of the armor was designed to free the cargo from the solution (Fig. S16(a)). As shown in Fig. S16(c), we can place steel ball cargos on the platform to realize cargo transportation.
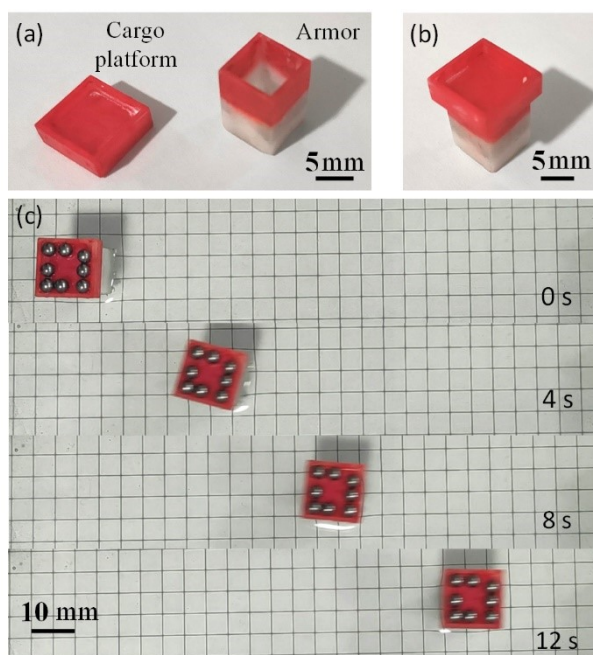
Fig. S16 A method for transporting cargos with a cargo platform. (a) The optical image of the cargo platform and armor. (b) Assembly diagram of cargo platform and armor. (c) The process of transporting cargos by a transport platform.

Besides, a new operating mechanical arm was explored and installed on the armor, as shown in Fig.S17(b). The main idea is to combine the rigid solid armor with external mechanical structures so that the motion of the LM under the electric field can be output and utilized. The mechanical structure transmitted power out of the solution to realize the cargo carrying function.

The working hand was used to transport drugs like methylene blue (MB) by synchronously controlling the movement of the vehicle (shown in Fig.S17(c)). In the process of MB transportation, a closed annular transport microchannel was made by polydimethylsiloxane (PDMS). One corner of the microchannel was placed with MB, and the other corner was 100 μL DI water droplet, as shown in Fig. S17(d). Under the action of the sAGV system, the vehicle moved in the glass container and transmitted the power to the PDMS microchannel through the mechanical arm. Since the LM vehicle would move along the electric field, the end of the operating hand would precisely transport the MB into the droplet along the microchannel outside the platform, as shown in Fig.S17(e).
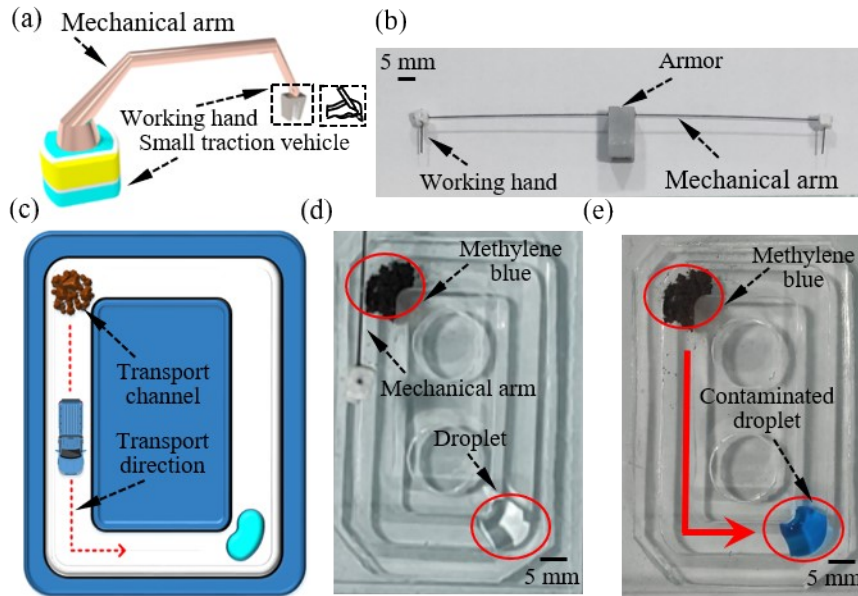
Fig. S17 Drugs transport function of the mechanical arm. (a) Structural design of the mechanical arm. (b) The physical picture of the experimental device. (c) Schematic of the good transport model. (d) State diagram before transportation. (e) The droplet is dyed blue after MB transportation.